https://doi.org/10.1038/s44304-025-00081-8

Urban subsidence zones prone to flooding: mitigated deformation trends post-2024 Guilin megaflood

Pinglang Kou[1,2], Xu Dong[1,2], Qiang Xu[3] ✉, Ali P. Yunus[4], Ying Xia[2], Yuxiang Tao[1], Rui Liu[5], Qin Ji[5], Ruikun Chen[1,2] & Zhengwu Yuan[1,2]

Climate change intensifies urban flood hazards, yet existing research often overlooks the complex dynamic relationships between surface deformation, soil properties, and flooding. This study uses the 2024 Guilin flood event as a case study, integrating SBAS-InSAR, DInSAR techniques, and various machine learning methods to explore the complex interactions between surface deformation, soil characteristics, and flooding. The results show that the flood caused significant water expansion, with ground subsidence mainly concentrated in the southern and eastern parts of Guilin, highly coinciding with the severely flooded areas. The flood-inundated areas exhibited opposite deformation trends before and after the flood, shifting from subsidence to uplift, while road subsidence also showed a dynamic process. Different machine learning methods showed varying performance in predicting surface deformation, with the ERT model performing relatively well. Soil thickness was positively correlated with surface subsidence within a certain range, and this relationship exhibited noticeable nonlinear characteristics post-flood. The findings of this study have important practical implications for urban flood mitigation, aiding urban planners in more accurately identifying flood-prone areas, especially those experiencing subsidence.

Flooding severely threatens urban areas worldwide, causing substantial economic losses and social disruptions[1–3]. As climate change intensifies, the frequency and magnitude of extreme weather events are escalating, elevating urban flood risks[4,5]. However, flood risk is intricately interwoven with multiple factors, including surface deformation, land-use alterations, and urbanization[6–8].

Recent studies have illuminated the complex, bidirectional relationship between surface subsidence and flooding[9–11]. Surface deformation, particularly subsidence, has become a critical factor influencing urban flood risk by altering topography and intensifying flood vulnerability[6,12,13]. Advanced remote sensing technologies, particularly Interferometric Synthetic Aperture Radar (InSAR), have revolutionized our ability to monitor surface deformation at large scales with high precision[14–16]. However, remote sensing data alone cannot fully comprehend and predict the complex relationship between surface deformation and flood risk.

Incorporating machine learning techniques in geosciences has opened new avenues for processing and analyzing vast, multi-source datasets, enhancing the accuracy of surface deformation predictions[17–19]. Soil characteristics, particularly thickness, role are crucial in surface deformation and flood risk dynamics[20–22]. Despite these advances, critical research gaps persist. Most studies focus on long-term deformation trends, neglecting short-term dynamic changes before and after flood events[11]. The dynamic evolution of the relationship between soil properties and surface deformation during flood events remains poorly understood[21].

Here we present a comprehensive analysis of the complex interactions between surface deformation, soil properties, and flooding, using the 2024 Guilin flood event as a case study. By integrating SBAS-InSAR and DInSAR techniques with various machine learning methods, we aim to quantify surface deformation characteristics before and after the flood, investigate the spatiotemporal impact of flooding on road infrastructure subsidence,

[1]Chongqing Engineering Research Center of Spatial Big Data Intelligent Technology, Chongqing University of Posts and Telecommunications, Chongqing, 400065, China. [2]Key Laboratory of Tourism Multisource Data Perception and Decision, Ministry of Culture and Tourism (TMDPD, MCT), Chongqing University of Posts and Telecommunications, Chongqing, 400065, China. [3]State Key Laboratory of Geohazard Prevention and Geoenvironment Protection, Chengdu University of Technology, Chengdu, Sichuan, 610059, China. [4]Department of Earth and Environmental Sciences, Indian Institute of Science Education and Research Mohali, Sahibzada Ajit Singh Nagar, Punjab, 140 306, India. [5]Chongqing Key Laboratory of GIS Application, School of Geography and Tourism, Chongqing Normal University, Chongqing, 401331, China. ✉e-mail: xq@cdut.edu.cn

analyze the nonlinear relationship between soil thickness and surface subsidence, and evaluate the potential of machine learning methods in predicting surface deformation.

Results

The study focused on Guilin City in northeastern Guangxi, spanning 109°36'50" to 111°29'30" East longitude and 24°15'23" to 26°23'30" North latitude (Fig. 1). With an area of 27,800 km² (11.74% of Guangxi) and a population of nearly 5 million, Guilin features a 'high on three sides, low in the center' topography and 1–3 km thick sediment layers with abundant karst groundwater[23]. Its complex geological structures and active karst processes make it prone to subsidence and collapse[24]. Guilin has a subtropical monsoon climate, with an average annual temperature of 19.1 °C and precipitation of 1887.6 mm over 166 days. As a major tourist destination, it has a developed transportation network (19,141 km of roads, including 833 km of highways). Frequent floods, including the largest since 1998 in June 2024, and ongoing urbanization make Guilin an ideal case study for analyzing surface deformation.

On June 19, 2024, Guilin City experienced its most severe flooding since 1998. The water level at the Guilin hydrological station peaked at 148.88 m at 00:55 on June 20, 2.88 m above the warning level (https://www.chinadaily.com.cn/). Satellite imagery analysis revealed significant hydrological changes, with extensive new water coverage in low-lying areas and regions proximal to major waterways (Supplementary Fig. 1). Using HEC-RAS, we simulated the flooding in Guilin City and generated a water depth map for 01:00 on June 20, 2024. Results indicated a maximum water depth of 49.33 m and an average depth of 9.48 m during the flood event (Supplementary Fig. 2). Water depths were lower in the western and northern parts of Guilin City, while the southern and eastern regions experienced greater depths. The relationship between simulated flood water depths and deformation rates for the two areas showed that water depths in Area 1 were primarily concentrated between 10 and 15 m, while Area 2 showed water

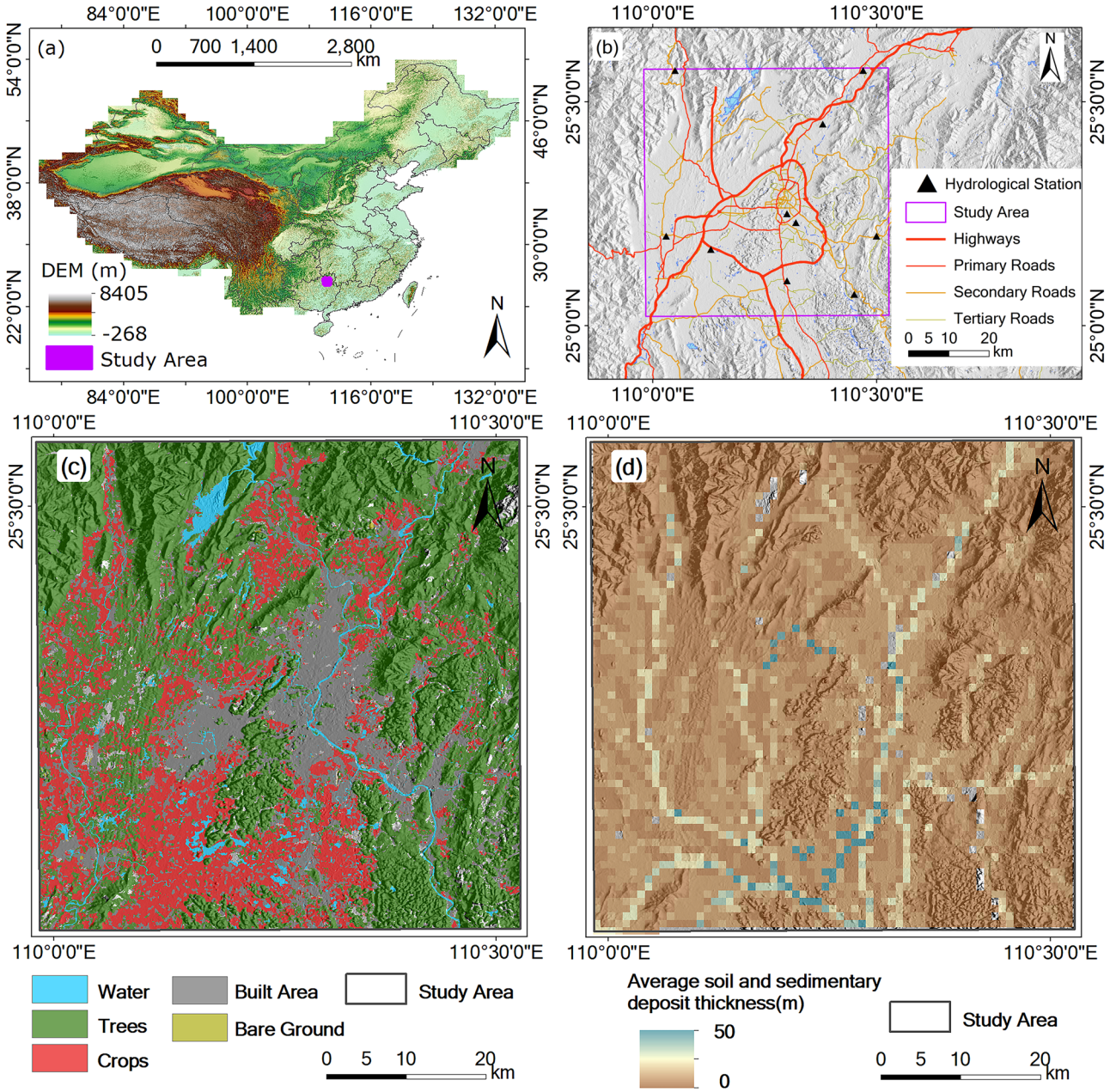

Fig. 1 | Map of the study area. a Location of the study area in China. **b** Distribution of roads within the study area. **c** Surface land cover of the study area. **d** Soil and sediment thickness in the study area. This map is generated using ArcGIS 10.7 with geographic information data.

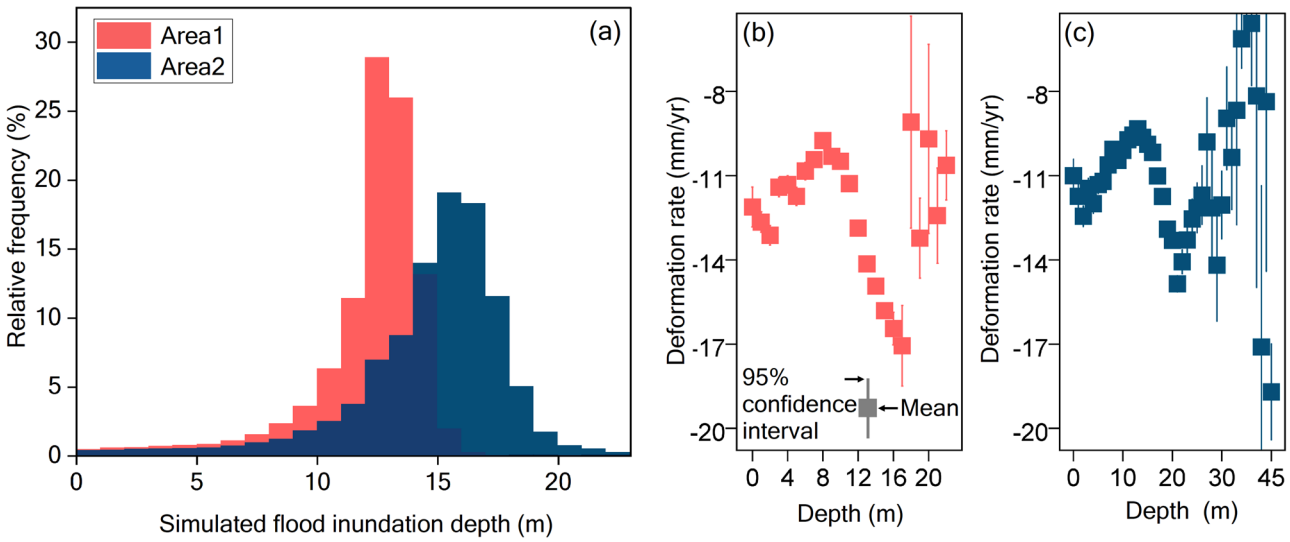

Fig. 2 | Relationship between simulated water depth and deformation rate. a Frequency distribution of simulated water depths in two areas; (**b**) Relationship between depth and deformation rate in Area 1. **c** Relationship between depth and deformation rate in Area 2. This map is generated using SPSS 20.

depths mainly distributed between 13 and 18 m (Fig. 2). Both areas exhibited a significant downward trend in deformation rates within their most common water depth ranges.

Our deformation rate analysis revealed significant spatial variations in ground subsidence rates across Guilin from June 2023 to June 2024 (Fig. 3). Severe subsidence areas were primarily concentrated in the southern and eastern parts of Guilin's urban area, while evident uplift was noted in the northwestern part. The maximum and minimum deformation rates were 151.62 mm/yr and −116.78 mm/yr respectively, with an average deformation rate of −1.18 mm/yr. Comparison of deformation rates between Areas 1–3 and the entire study area (Supplementary Table 1) showed that Areas 1 and 2 had significantly lower maximum rates than the study area, while Area 3 experienced an overall uplift trend. Cumulative deformation analysis from June 2023 to June 2024 (Supplementary Fig. 3) showed a consistent pattern with the subsidence rate distribution.

Analysis of two post-flood periods (May 27 to July 14, 2024, and May 27 to July 26, 2024) revealed significant spatial variations in subsidence, with severe subsidence in eastern Lingui District, northwestern Lingchuan County, and Xiufeng District (Fig. 4). Areas 1 and 2 exhibited post-flood uplift, reversing pre-flood subsidence trends. All three inundated areas showed uplift post-flooding (Supplementary Tables 2 and 3).

SBAS InSAR calculations within a 30 m buffer zone along roads revealed severe road subsidence in the southern region, coinciding with the primary inundated areas (Fig. 5). During the first phase after the flood (May 27, 2024, to July 14, 2024), a significant overall surface uplift of 28.11 ± 19.24 mm was observed. The period from May 27, 2024, to July 26, 2024, showed a mitigated ground uplift, with a deformation magnitude of 19.64 ± 31.36 mm.

Surface deformation models using SVM, GBDT, RF, ERT, and LSTM were trained on SBAS-InSAR results. The ERT model performed best in Area 1 (RMSE = 5.39, $R^2 = 0.72$) and achieved near-perfect predictions in Area 2 (RMSE ≈ 0, $R^2 = 0.99$) (Supplementary Figs. 4 and 5). Pre-flood SBAS-InSAR and post-flood DInSAR data (Fig. 6) revealed a shift from gradual subsidence to slight uplift in Areas 1 and 2 post-flood.

Analysis revealed a positive correlation between soil thickness and surface subsidence rates, particularly in areas with soil thickness ranging from 0 to 3 m (Supplementary Fig. 6). After the flood, the relationship between soil thickness and surface deformation showed significant differences in the two periods. In the first stage (May 27, 2024, to July 14, 2024), there was no significant correlation, while in the second stage (May 27, 2024, to July 26, 2024), soil thickness and surface deformation showed polarized characteristics.

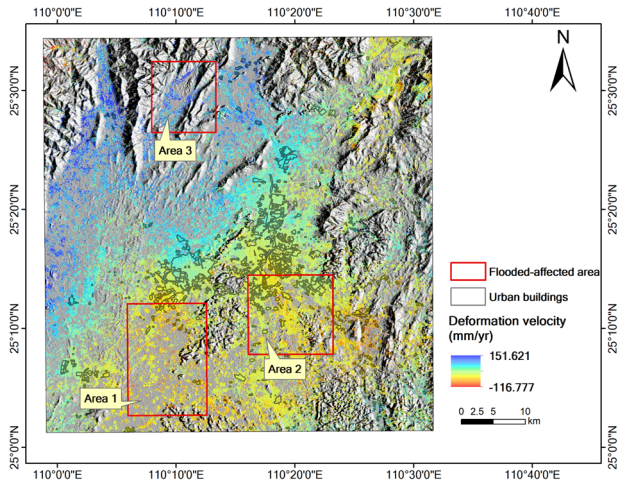

Fig. 3 | The deformation rate map was generated using Sentinel-1A data from June 2, 2023, to May 27, 2024. The flood inundation areas on June 20, 2024, are marked with red boxes, and urban buildings in Guilin are indicated by gray boxes. This deformation map is generated using ENVI 5.6 with the SarScape 5.6.2 module for data analysis and visualized using ArcGIS 10.7.

Discussions

This study revealed the significant impact of floods on surface deformation through remote sensing monitoring and analysis of the 2024 Guilin flood event. The flood caused significant water body expansion, particularly in low-lying areas and regions close to major rivers (Supplementary Fig. 1). Ground subsidence was mainly concentrated in the southern and eastern regions of Guilin, highly coinciding with the most severely flooded areas (Fig. 3). As the ground surface gradually sinks, it creates local depressions that naturally collect and retain water during flood events. These subsidence-induced basins effectively lower the flood threshold in affected areas, making them more susceptible to inundation during rainfall events. The discrepancy between the HEC-RAS simulated maximum water depth (49.33 m) and the peak water level recorded at the Guilin hydrological station (148.88 m) stems from different measurement references. While temporal consistency in flood peaks and processes supports the simulation's reliability, the differences highlight limitations in the model's ability to capture absolute water depths accurately. Future work should integrate additional hydrological data to improve simulation accuracy. Future studies

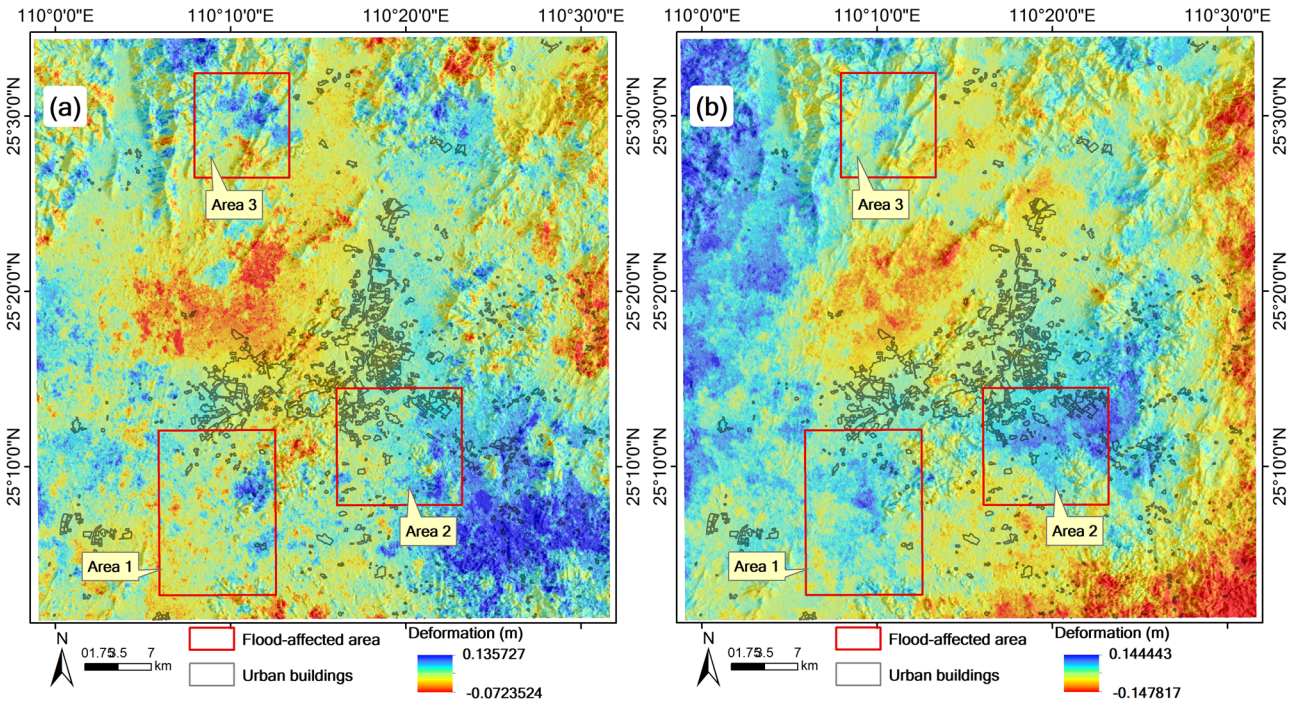

Fig. 4 | Deformation maps were generated using Sentinel-1A data. a Deformation from May 27, 2024, to July 14, 2024. **b** Deformation from May 27, 2024, to July 26, 2024. The surface deformation map is created using ENVI 5.6 with the SarScape 5.6.2 module for data analysis and visualized using ArcGIS 10.7.

should integrate hydrological station data to further refine flood simulation models and enhance prediction accuracy. This finding aligns with previous research identifying surface subsidence as a contributing factor to floods with spatial heterogeneity in its impact[25].

The flood-inundated areas exhibited a reversal in deformation trends post-flood, shifting from subsidence to uplift (Fig. 4). This suggests that flood events can temporarily alter local surface deformation patterns[19,21]. However, the observed changes may be influenced by short-term factors such as soil saturation and groundwater fluctuations, and longer-term monitoring is needed to determine whether these trends persist. Before the flood event, Areas 1 and 2 showed a subsidence trend, which may be due to factors in the urbanization process such as excessive groundwater extraction, land use changes, and increased urban infrastructure load[26]. Similar surface deformation patterns have been reported in other studies. For instance, Le Mouélic et al.[27] observed ground uplift associated with changes in groundwater levels in Paris. Additionally, flooding in abandoned coal mining areas can lead to ground uplift[28]. The sudden trend reversal may be due to multiple mechanisms, including soil saturation, increased buoyancy due to rising groundwater levels, and soil reconsolidation during the subsequent water level decline and soil drainage process. We found the dynamic process of road subsidence after the flood, with initial surface uplift followed by gradual and intensifying subsidence (Fig. 5). This process may result from multiple factors, including changes in soil structure, groundwater level fluctuations, and load redistribution. These findings are consistent with observations of complex changes in road connectivity over time after flood events[22].

Various machine learning methods were employed to predict surface deformation, reflecting the widespread application trend in earth science research. The ERT model showed better prediction accuracy in both study areas, potentially due to its introduction of greater randomness in the tree construction process (Supplementary Figs. 4 and 5). However, the generally low prediction accuracy of most models highlights the importance of long-term InSAR data for improving surface deformation prediction accuracy[12,29].

The results highlighted the long-term impact of floods on road infrastructure, providing a baseline for flood-induced subsidence (Fig. 6). This is critical for infrastructure maintenance and disaster prevention strategies, as noted in urban subway system studies[30]. The study revealed an approximate positive correlation between soil thickness and surface subsidence, especially in the 0–3 m thickness range (Supplementary Fig. 6a). This finding is consistent with observations of more significant subsidence in areas with thicker soil layers[31]. The study also found that more than 60% of the soil thickness in the study area is concentrated in the 0–5 m range (Supplementary Fig. 6d), emphasizing the importance of focusing on specific thickness ranges in urban planning and flood risk assessment.

Within the main distribution interval of soil thickness (0–5 m) (Supplementary Fig. 6d), surface deformation after the flood showed obvious nonlinear characteristics (Supplementary Fig. 6a–c). In the first stage after the flood, there was no significant correlation between soil thickness and surface deformation, possibly due to general soil saturation. In the second stage, the relationship showed polarized characteristics, reflecting different responses of soil layers of varying thicknesses to floods. These findings align with recent research highlighting the complex nature of urban flood risk, particularly the impacts of repeated, localized flooding events on long-term economic outcomes[32]. The observed nonlinear relationship between soil thickness and surface deformation is consistent with studies on mining subsidence in areas with thick alluvium, where surface subsidence is influenced by multiple factors including alluvium thickness, internal friction angle, and cohesive force[33]. Similarly, research in coal mining areas with thick alluvium has shown that surface subsidence is a complex process involving interactions between bedrock, alluvium soil, groundwater, and shallow soil compaction[34]. The observed nonlinear relationships underscore the need for adaptive strategies in flood-prone urban areas, including reconsidering development incentives in high-risk zones[35]. Future research should explore the influence of other factors (such as soil type, and groundwater dynamics) on this nonlinear relationship to build a more comprehensive urban flood disaster impact assessment model.

The findings of this study have significant practical implications for urban flood mitigation. By considering the complex relationships between surface deformation, soil characteristics, and flooding, our multi-dimensional assessment method helps urban planners more accurately identify flood-prone areas, especially those experiencing subsidence.

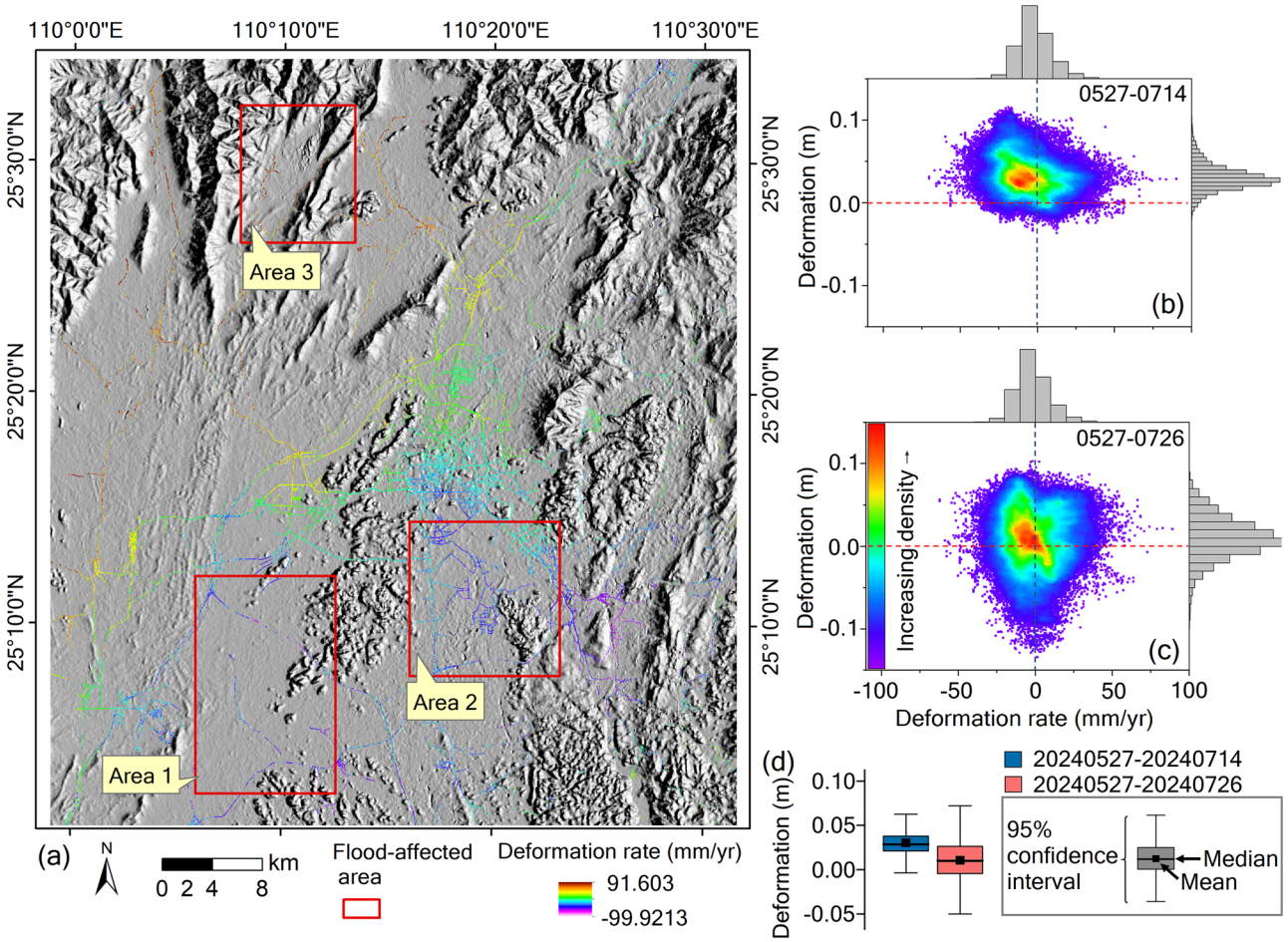

Fig. 5 | Deformation characteristics along roads within a 30 m buffer zone in the study area. a Deformation rate along roads within the 30 m buffer zone. **b** Deformation from May 27, 2024, to July 14, 2024, after the flood. **c** After the flood, the deformation from May 27, 2024, to July 26, 2024. **d** Deformation from May 27, 2024, to July 14, 2024, and from May 27, 2024, to July 26, 2024, after the flood. Road deformation characteristics are generated using ENVI 5.6 with the SarScape 5.6.2 module for data analysis and visualized using ArcGIS 10.7.

However, the study's reliance on a single flood event and limited InSAR data restricts the generalizability of the results. Future research should incorporate additional case studies and datasets to validate and refine these findings. This study has limitations, including the restricted period of InSAR data and reliance on a single flood event in Guilin. Differences between simulated and observed water levels highlight model limitations. Future research should incorporate more hydrological data, explore additional factors like groundwater dynamics and land use changes, and extend to various urban environments for a comprehensive understanding of urban flood impacts.

Methods

The study utilized high-resolution radar imagery data from Sentinel-1A provided by the Alaska Satellite Facility, combined with various related data from Guilin City, to systematically analyze ground subsidence in the study area. Sentinel-1A satellite is an important Earth observation satellite in the European Space Agency's Copernicus program (GMES), with a 12-day revisit cycle and an orbital height of 693 km. The study used 29 ascending orbit images acquired from June 2023 to June 2024, using VV single polarization mode and IW imaging mode, covering an area of approximately 3413 km^2, encompassing most of Guilin's urban area. During data processing, ENVI software was used to analyze ground subsidence, and a 30 m resolution digital elevation model (DEM) obtained from the Geospatial Data Cloud was used for removing interference phases and geocoding. Additionally, precise orbit data from the European Space Agency was used to improve processing accuracy. To further analyze the causes of ground subsidence, related information about Guilin City was collected, including rainfall data, road network data, land cover data, and soil and sediment thickness data. These data were sourced from the GRIP road dataset (www.globio.info/download-grip-dataset), Esri land cover data, sediment thickness data produced by NASA DACC, urban building data, and precipitation data from the Japan Aerospace Exploration Agency (JAXA) (https://sharaku.eorc.jaxa.jp/GSMaP/). The comprehensive use of these multi-source data provided important support for a comprehensive assessment of the spatiotemporal characteristics of ground subsidence in Guilin City. The study used SBAS-InSAR technology to process Sentinel-1A radar imagery data before the flood to obtain surface deformation detection results, and DInSAR technology to process imagery data before and after the flood to obtain surface deformation results under flood impact. Then, machine learning techniques were used to train models using the results obtained from SBAS-InSAR to simulate surface deformation results without flood impact, which were compared with DInSAR results (Supplementary Fig. 7).

Differential Interferometric Synthetic Aperture Radar (DInSAR) technology was the key method used in this study to analyze surface deformation in Guilin City before and after the flood. The two-pass method was adopted, selecting pre-flood imagery as the master image and post-flood imagery as the slave image. First, residual phase maps were generated through registration and multi-looking processing, followed by adaptive filtering to reduce noise while generating coherence maps. After phase map filtering, the minimum cost flow algorithm was used for phase unwrapping, with a coherence threshold set at 0.2. This threshold balances information retention in flood-affected areas with reliable phase unwrapping. To

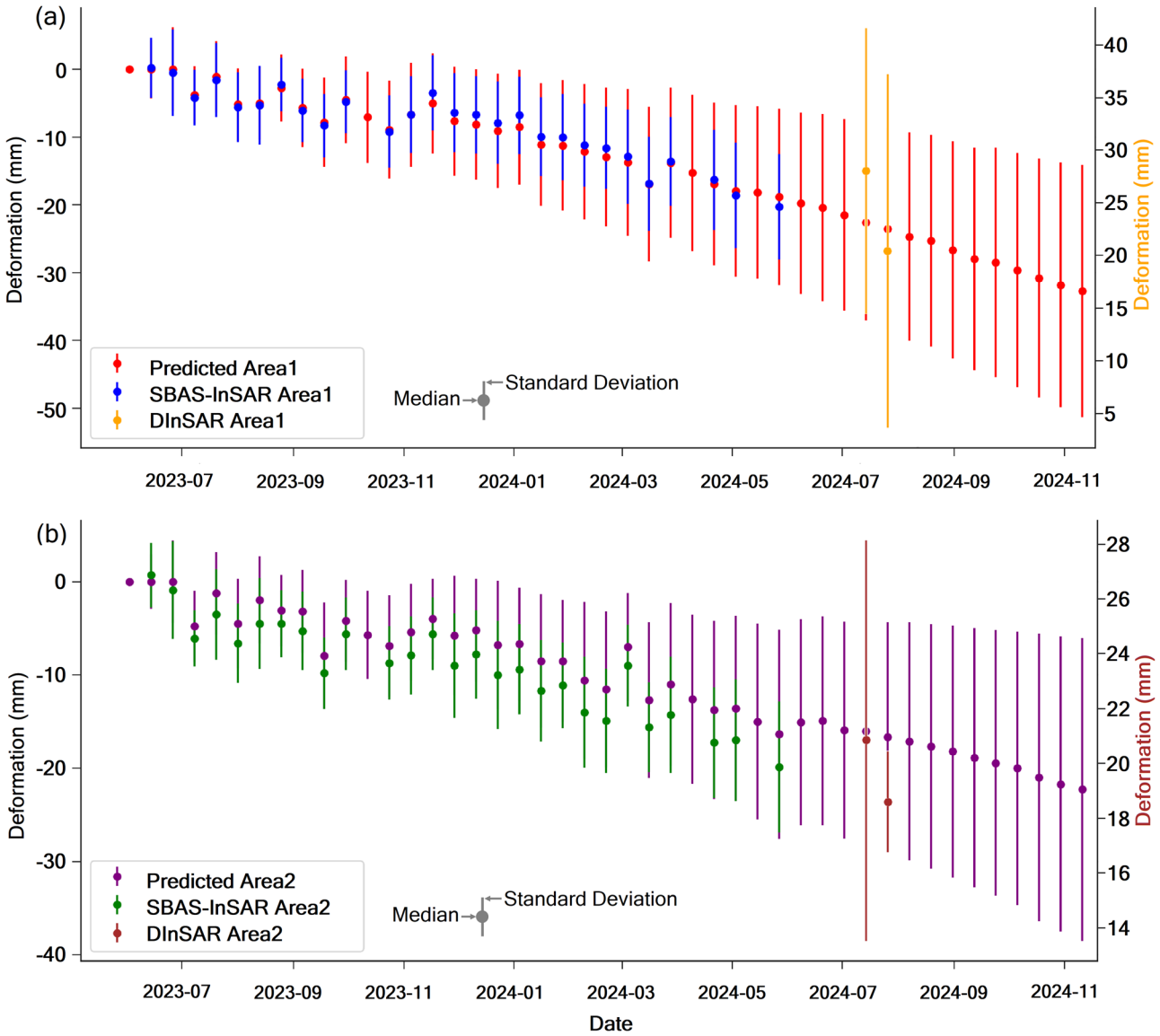

Fig. 6 | Comparison of pre-flood SBAS-InSAR (June 14, 2023, to May 27, 2024), two post-flood DInSAR periods (May 27 to July 14, 2024, and May 27 to July 26, 2024), and predicted deformation based on SBAS-InSAR for two areas (June 2, 2023, to November 23, 2024). Graphs (**a**) and (**b**) represent areas 1 and 2 respectively. The dot represents the median, and the error bar represents the standard deviation. The right Y-axis shows the D InSAR data. The data visualization is performed using SPSS 20.

improve accuracy, 7 orbit refinement ground control points were manually inserted in areas with little deformation and flat terrain for orbit refinement and re-flattening processing. The principles for selecting control points included choosing areas with minimal expected deformation, high coherence (>0.8), uniform distribution, and avoiding water bodies and vegetation areas. Some studies also evaluated the stability of control points within a 20-m radius around candidate points to ensure the reference points remain stable during the monitoring period[36]. Finally, referring to the digital elevation model (DEM), phase information in the radar coordinate system was converted to deformation information in the geographic coordinate system, and coding was completed. Through this series of steps, surface deformation data for Guilin City under flood impact from May 27, 2024, to July 14, 2024, and from May 27, 2024, to July 26, 2024, were successfully extracted, providing an important basis for flood impact assessment. We specifically analyzed two post-flood periods to capture the dynamic evolution of surface deformation in the short-term aftermath of the flood event. This dual-period approach allows us to assess both the immediate impact of the flood and any subsequent changes or stabilization in deformation patterns, providing insights into the area's response and recovery process following the flood.

For the pre-flood analysis, we chose to use SBAS-InSAR technology. While Persistent Scatterer Interferometry (PSI) and SqueeSAR techniques are often favored in urban areas, we selected SBAS-InSAR for its ability to handle both distributed and point-like scatterers, which was crucial for our mixed urban-rural study area[37]. SBAS-InSAR offered better coverage in areas with lower coherence, such as those affected by floods, and could capture non-linear deformation more effectively[38]. However, the presence of atmospheric water vapor during flood events can exacerbate phase noise, reducing coherence and complicating deformation analysis[14,38]. It also provided a smoother displacement time series, which was essential for analyzing complex surface changes before and after flood events. Using ENVI's Sarscape plugin, 29 SAR image data sets from June 2023 to June 2024 were processed. First, a connection graph was generated, selecting the image from November 17, 2023, as the super master image, with a time baseline threshold of 120 days and a spatial baseline threshold of 5% of the total. Subsequently, comprehensive interference processing was performed, including interferogram generation, flattening, adaptive filtering (using Goldstein algorithm, with a multi-look ratio of 4:1), coherence coefficient generation, phase unwrapping (coherence threshold of 0.15, using minimum cost flow algorithm), and automatic orbit refinement and re-

flattening. This low threshold was chosen to retain more information in Guilin's diverse terrain. In the first inversion, the deformation rate and residual terrain were estimated, followed by secondary phase unwrapping to optimize results. The second inversion focused on calculating displacements in the time series and performing customized atmospheric filtering to remove atmospheric phase interference. Finally, results were converted to the geographic coordinate system concerning the DEM. Through this series of complex processing steps, detailed surface deformation information for Guilin City from June 2023 to June 2024 was successfully extracted, laying the foundation for assessing the long-term impact of floods on surface structures. The study used various machine learning techniques to build surface deformation prediction models, including Support Vector Machine (SVM), Gradient Boosting Decision Tree (GBDT), Random Forest (RF), Extremely Randomized Tree (ERT), and Long Short-Term Memory (LSTM) methods. In a specific implementation, the SVM sought an optimal hyperplane for classification by maximizing the margin between categories, thereby improving classification accuracy and solving regression problems. The GBDT gradually combined multiple decision tree models to correct errors, progressively improving overall prediction performance. The RF constructed multiple decision trees and performed voting or averaging, reducing overfitting phenomena and improving model stability. The ERT introduced greater randomness in the tree construction process, further enhancing the model's generalization ability. The LSTM is an improved recurrent neural network the RNN that, compared to traditional RNNs, solved the problems of gradient vanishing and gradient explosion in long sequences by introducing gating mechanisms (input gate, forget gate, and output gate), thereby effectively capturing long-term dependencies. In the construction process of these models, cross-validation was performed to ensure the reliability of results and the robustness of the models.

Additionally, the best-performing machine learning model was used to conduct detailed deformation predictions for two significant deformation areas (Area1 and Area2). Specifically, these two local areas were selected from the flood-inundated areas, We used SBAS-InSAR to obtain cumulative subsidence data from 29 scenes between June 2, 2023, and May 27, 2024. Seventy percent of this data was used as a training set to train the model, and thirty percent was used as a test set to evaluate the model's performance. The trained model was then used to predict cumulative subsidence data from 15 scenes between June 8, 2024, and November 23, 2024. Through this method, not only could the model's prediction performance be evaluated, but valuable insights could also be provided for future surface deformation trends.

This study used the Google Earth Engine (GEE) platform to extract changes in water bodies before and after the 2024 Guilin flood, analyzing Sentinel-1A radar imagery. First, the study area was defined, which delineated the flood risk area of Guilin City through latitude and longitude coordinates. Then, Sentinel-1A images before (May 27, 2024) and after (June 20, 2024) the flood were obtained from GEE, filtering VV polarization data, and averaging images within the selected time range to reduce random errors in single images. By calculating pixel value differences between the two periods of images, a different image was generated to identify flood areas. To ensure accurate extraction of flood areas, a threshold of 1.25 was set, identifying possible flood areas through high-value regions in the different images. Finally, pre- and post-flood images and identified flood areas were visualized on the GEE platform, and the newly added water body area caused by the flood was calculated. This method achieved rapid identification and quantitative assessment of flood disaster areas through efficient radar image analysis, providing an important decision-making basis for post-disaster emergency response. Additionally, to analyze the impact of floods on different areas in depth, three typical flood-inundated areas (Area 1, Area 2, and Area 3) were selected for detailed study. The deformation rates of these areas were compared with those of the entire study area, including maximum rate, minimum rate, and average rate. Through this comparison, the degree of impact of floods on surface deformation under different geographical locations and geological conditions could be quantified.

Multiple InSAR techniques combined with machine learning prediction methods were used to comprehensively analyze the impact of floods on surface deformation and compare deformation before and after the flood. First, SBAS-InSAR technology was used to process Sentinel-1A data from June 2, 2023, to May 27, 2024, obtaining a time series of surface deformation before the flood. Subsequently, DInSAR technology was used to process data from May 27, 2024, to July 14, 2024, and from May 27, 2024, to July 26, 2024, respectively, obtaining surface deformation conditions for two periods after the flood. At the same time, based on SBAS-InSAR results, the best-performing machine learning model was used to predict surface deformation for two typical areas (Area1 and Area2) within the study area, with the prediction period extending from June 2, 2023, to November 23, 2024. This prediction result represented the theoretical deformation trend without flood impact.

To further understand the impact of floods on surface deformation, the HEC-RAS numerical simulation software was used to simulate floods in the study area. We employed the HEC-RAS software, specifically its 2D Flow Model. Based on the Saint-Venant equations, this model is particularly suitable for handling complex terrains and urban flood management scenarios. We imported the Digital Elevation Model (DEM) of the study area, selected a 2D flow area slightly larger than the study area, divided it into 6778 grid cells, and applied a default Manning's roughness coefficient of 0.06. The simulation time range was from 0:00 on June 19, 2024, to 1:00 on June 20, 2024, which was also the observed peak rainfall period. The simulation used an hourly time resolution to capture the dynamic changes in rainfall intensity and flood evolution. In this way, surface deformation data could be compared with flood simulation results, leading to a more comprehensive understanding of the impact of flood events on surface deformation. To visually compare the differences before and after the flood and prediction results, SBAS-InSAR, DInSAR, machine learning prediction results, and flood simulation results were integrated. By analyzing changes in the median of deformation and the distribution of water depth from flood simulation, the continuous subsidence trend before the flood, the predicted theoretical subsidence continuation, and the sudden change in surface deformation after the flood could be observed, while also assessing the differential impact of floods on surface deformation in different areas. To analyze the relationship between flood inundation depth and surface deformation, simulation and data analysis were conducted for two flood-inundated areas (Area 1 and Area 2). First, a hydrological model was used to simulate flood inundation depth, and the relative frequency distribution of water depth was calculated. This allowed us to identify the most likely range of flood depths experienced in each area. Second, by comparing the deformation in these two areas with the simulated flood inundation depths, we paired flood depth data with deformation rate data to explore potential associations between the two. For each area, we paid particular attention to deformation characteristics within the most common flood depth range.

To assess the impact of soil thickness on ground subsidence before and after the flood, this study used results calculated from both SBAS InSAR and DInSAR technologies for pre- and post-flood deformation monitoring. First, based on SBAS InSAR technology, we calculated the surface deformation rate before the flood occurred to explore the potential relationship between soil thickness and deformation rate. The time series of SBAS InSAR covered a long period, allowing us to identify long-term trends of surface deformation in soil layers of different thicknesses. Next, we applied DInSAR technology to calculate surface deformation before and after the flood, specifically for the periods from May 27, 2024, to July 14, 2024, and from May 27, 2024, to July 26, 2024. The DInSAR results allowed us to capture surface deformation characteristics in the short time before and after the flood event. Additionally, by analyzing the frequency distribution of soil thickness and deformation rates, we further revealed the spatial distribution characteristics of soil thickness at different deformation stages. Through the combination of these methods, we were able to explore the role of soil thickness in surface subsidence before and after the flood.

Data availability

The SBAS InSAR-derived ground deformation time series (GeoTIFF format, 2020-2024), predicted subsidence models for subregions 1/2, and two-phase D-InSAR-derived post-flood deformation data (27 May - 26 July 2024 and 27 May - 14 July 2024) are publicly available in the Zenodo repository (https://sandbox.zenodo.org/records/165115?preview=1&token=eyJhbGciOiJIUzUxMiJ9.eyJpZCI6IjQ5YmY0MTM4LTAyNmUtNDBlNC1hOTA1LTk4MWE2MDk1Njc0MiIsImRhdGEiOnt9LCJyYW5kb20iOiI0YTdmNWFmNDRmN2NiM2QwN2ZlYjczOWJhZjY1ZmYyYyJ9.SV9oQlGsj5l75_zXparwuO2Se8N3PlD-J9tM0VaxI4z-DMfsS2l2A_lwLaTp5XSK5qWyogz2hro2-smHVyfmWA).

Received: 8 September 2024; Accepted: 28 February 2025;
Published online: 03 April 2025

References

1. Aerts, J. C. et al. Evaluating flood resilience strategies for coastal megacities. *Science* **344**, 473–475 (2014).
2. Jongman, B., Ward, P. J. & Aerts, J. C. Global exposure to river and coastal flooding: Long term trends and changes. *Glob. Environ. Change* **22**, 823–835 (2012).
3. Kreibich, H., Bubeck, P., Van Vliet, M. & De Moel, H. A review of damage-reducing measures to manage fluvial flood risks in a changing climate. *Mitig. Adapt. Strateg. Glob. Change* **20**, 967–989 (2015).
4. Hsiao, S.-C. et al. Flood risk influenced by the compound effect of storm surge and rainfall under climate change for low-lying coastal areas. *Sci. Total Environ.* **764**, 144439 (2021).
5. Di Traglia, F. et al. Tracking morphological changes and slope instability using spaceborne and ground-based SAR data. *Geomorphology* **300**, 95–112 (2018).
6. Chen, B. et al. Characterization and causes of land subsidence in Beijing, China. *Int. J. Remote Sens.* **37**, 2129–2147 (2016).
7. Zhou, C. et al. Quantifying the contribution of multiple factors to land subsidence in the Beijing Plain, China with machine learning technology. *Geomorphology* **335**, 48–61 (2019).
8. Solari, L. et al. From ERS 1/2 to Sentinel-1: Subsidence monitoring in Italy in the last two decades. *Front. Earth Sci.* **6**, 149 (2018).
9. Fiaschi, S. & Wdowinski, S. Local land subsidence in Miami Beach (FL) and Norfolk (VA) and its contribution to flooding hazard in coastal communities along the U.S. Atlantic coast. *Ocean Coast. Manag.* **187**, 105078 (2020).
10. Jiang, H. et al. Does flooding get worse with subsiding land? Investigating the impacts of land subsidence on flood inundation from Hurricane Harvey. *Sci. Total Environ.* **856**, 161072 (2023).
11. Navarro-Hernández, M. I. et al. Analyzing the impact of land subsidence on the flooding risk: Evaluation through InSAR and modeling. *Water Resour. Manag.* **37**, 1857–1873 (2023).
12. Wang, G. et al. Flood risk assessment of subway systems in metropolitan areas under land subsidence scenario: A case study of Beijing. *Remote Sens.* **13**, 637 (2021).
13. Zhou, R., Zheng, H., Liu, Y., Xie, G. & Wan, W. Flood impacts on urban road connectivity in southern China. *Sci. Rep.* **12**, 17119 (2022).
14. Berardino, P., Fornaro, G., Lanari, R. & Sansosti, E. A new algorithm for surface deformation monitoring based on small baseline differential SAR interferograms. *IEEE Trans. Geosci. Remote Sens.* **40**, 2375–2383 (2002).
15. Ferretti, A., Prati, C. & Rocca, F. Permanent scatterers in SAR interferometry. *IEEE Trans. Geosci. Remote Sens.* **39**, 8–20 (2001).
16. Hooper, A., Bekaert, D., Spaans, K. & Arıkan, M. Recent advances in SAR interferometry time series analysis for measuring crustal deformation. *Tectonophysics* **514**, 1–13 (2012).
17. Dramsch, J. S. 70 years of machine learning in geoscience in review. *Adv. Geophys.* **61**, 1–55 (2020).
18. Kumar, S., Kumar, D., Donta, P. K. & Amgoth, T. Land subsidence prediction using recurrent neural networks. *Stoch. Environ. Res. Risk Assess.* **36**, 1359–1371 (2022).
19. Qiao, X. et al. Interpretation and attribution of coastal land subsidence: An InSAR and machine learning perspective. *IEEE J. Sel. Top. Appl. Earth Obs. Remote Sens.* **17**, 804–815 (2024).
20. Wang, J. et al. A prediction method for surface subsidence at deep mining areas with thin bedrock and thick soil layer considering consolidation behavior. *Nat. Resour. Res.* **33**, 335–350 (2024).
21. Yao, Y., Ni, J. & Li, J. Stress-dependent water retention of granite residual soil and its implications for ground settlement. *Comput. Geotech.* **129**, 103835 (2021).
22. Zhang, X. et al. Active layer thickness retrieval over the Qinghai-Tibet Plateau using Sentinel-1 multitemporal InSAR monitored permafrost subsidence and temporal-spatial multilayer soil moisture data. *IEEE Access* **8**, 110910–110923 (2020).
23. Yu, G. et al. The Urban Underground Space beneath the Karst Basin of Guilin, China, Revealed by Ambient Seismic Noise Tomography. *Seismol. Soc. Am.* **94**, 172–188 (2023).
24. Dai, J., et al. An assessment of karst collapse hazards in Guilin, Guangxi Province, China. In: *Sinkholes and the Engineering and Environmental Impacts of Karst*, 156–164 (A.A. Balkema Publishers, 2008).
25. Mehrabi, A. Monitoring the Iran Pol-e-Dokhtar flood extent and detecting its induced ground displacement using Sentinel-1 imagery techniques. *Nat. Hazards* **106**, 1589–1606 (2021).
26. Samsonov, S., d'Oreye, N. & Smets, B. Ground deformation associated with post-mining activity at the French–German border revealed by novel InSAR time series method. *Int. J. Appl. Earth Obs. Geoinf.* **23**, 142–154 (2013).
27. Le Mouélic, S. et al. A ground uplift in the city of Paris (France) detected by satellite radar interferometry. *Geophys. Res. Lett.* **29**, 34–1 (2002).
28. Zhao, J. & Konietzky, H. An overview on flooding induced uplift for abandoned coal mines. *Int. J. Rock Mech. Min. Sci.* **148**, 104955 (2021).
29. Chen, M. et al. Imaging land subsidence induced by groundwater extraction in Beijing (China) using satellite radar interferometry. *Remote Sens.* **8**, 468 (2016).
30. Zhang, Y. et al. Long-term subsidence in Mexico City from 2004 to 2018 revealed by five synthetic aperture radar sensors. *Land Degrad. Dev.* **31**, 1306–1321 (2020).
31. Chai, L. et al. Risk assessment of land subsidence based on GIS in the Yongqiao area, Suzhou City. *China. Sci. Rep.* **14**, 11377 (2024).
32. Costa, R. et al. Repeated and localized flooding is an underestimated challenge for urban disaster risk management. *Nat. Cities* **1**, 587–596 (2024).
33. Zhao, G., Guo, W. & Li, X. Mechanical properties of mega-thick alluvium and their influence on the surface subsidence. *Geotech. Geol. Eng.* **38**, 137–149 (2020).
34. Zhou, D. W. et al. Mechanism of mining subsidence in coal mining area with thick alluvium soil in China. *Arab. J. Geosci.* **8**, 1855–1867 (2015).
35. Druckenmiller, H. et al. Removing development incentives in risky areas promotes climate adaptation. *Nat. Clim. Chang.* **14**, 1–9 (2024).
36. Ramirez, R. A., Abdullah, R. E. E. & Rubio, C. J. P. S1-PSINSAR monitoring and hyperbolic modeling of nonlinear ground subsidence in Naga City, Cebu Island in the Philippines. *GEOMATE J.* **23**, 102–109 (2022).
37. Zhang, P. et al. Land subsidence monitoring method in regions of variable radar reflection characteristics by integrating PS-InSAR and SBAS-InSAR techniques. *Remote Sens.* **14**, 3265 (2022).
38. Chen, X. et al. Comparison between PS and SBAS InSAR techniques in monitoring shallow landslides. *Underst. Reduc. Landslide Disaster Risk* **5**, 155–161 (2021).

Acknowledgements
This work was supported by the National Key Research and Development Program of China (2022YFC3003205), the Opening fund of State Key Laboratory of Geohazard Prevention and Geoenvironment Protection (Chengdu University of Technology) (SKLGP2023K008), Natural Science Foundation of Chongqing Municipal Science and Technology Commission (CSTB2023NSCQ-MSX0990), and the Hebei Natural Science Foundation (D2023403055).

Author contributions
P.L.K. and Z.W.Y. conceptualized the research framework; X.D. and Y.X.T. developed the SBAS InSAR processing workflow; Q.X. (Corresponding Author) designed the validation experiments and supervised the study; A.P.Y. performed a comparative analysis with hydrological datasets; Y.X. conducted time-series deformation extraction; R.L. provided geospatial data infrastructure support; Q.J. implemented the subsidence prediction models; R.K.C. analyzed urban infrastructure impacts; All authors participated in result interpretation, manuscript revision, and approved the final version.

Competing interests
The authors declare no competing interests.

Additional information
Supplementary information The online version contains supplementary material available at https://doi.org/10.1038/s44304-025-00081-8.

Correspondence and requests for materials should be addressed to Qiang Xu.